ACS APPLIED MATERIALS & INTERFACES

Research Article

www.acsami.org

First-Principles Calculations of Oxygen Vacancy Formation and Metallic Behavior at a β-MnO_2 Grain Boundary

James A. Dawson,*[,†] Hungru Chen,[‡] and Isao Tanaka[†]

[†]Department of Materials Science and Engineering, Kyoto University, Sakyo, Kyoto 606-8501, Japan

[‡]Environmental Remediation Materials Unit, National Institute for Materials Sciences, Tsukuba, Ibaraki 305-0044, Japan

ABSTRACT: Nanostructured MnO_2 is renowned for its excellent energy storage capability and high catalytic activity. While the electronic and structural properties of MnO_2 surfaces have received significant attention, the properties of the grain boundaries (GBs) and their contribution to the electrochemical performance of the material remains unknown. Through density functional theory (DFT) calculations, the structure and electronic properties of the β-MnO_2 Σ 5(210)/[001] GB are studied. Our calculations show this low energy GB has a significantly reduced band gap compared to the pristine material and that the formation of oxygen vacancies produces spin-polarized states that further reduce the band gap. Calculated formation energies of oxygen vacancy defects and Mn reduction at the GB core are all lower than the equivalent bulk value and in some cases lower than values recently calculated for β-MnO_2 surfaces. Oxygen vacancy formation is also shown to produce a metallic behavior at the GB with defect charge distributed over a number of oxygen and manganese sites. The low energies of oxygen defect formation and the potential creation of conductive GB pathways are likely to be important to the electrochemical performance of β-MnO_2.

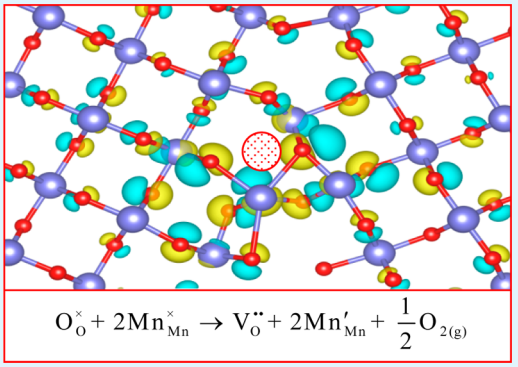

KEYWORDS: *cathode material, grain boundaries, catalyst, lithium battery, supercapacitor*

1. INTRODUCTION

The need for materials with higher energy capacity and storage for various applications including hybrid electric vehicles and renewable energy sources is an ongoing issue in materials and energy science. Many conventional battery and catalytic materials have significant disadvantages, for example, the cost of $LiCoO_2$ and the difficulty in its disposal. Whereas β-MnO_2 as an electrode material and catalyst is easy to prepare, low in cost and low in toxicity.[1] The search for safer, cheaper and more efficient energy storage materials has resulted in considerable research of manganese oxides in recent years.[2−4]

One of the most important applications of β-MnO_2 is as a cathode in Li-ion batteries, although studies of bulk β-MnO_2 show no significant Li-ion intercalation[5,6] as a likely result of the narrow tunnels present in the rutile structure.[4] More recent studies show that nanocomposite and mesoporous β-MnO_2 samples possess good Li-ion intercalation,[7,8] high capacities[5,7,9] of up to 320 mAh g^{-1} and good cycling stability.[5] In addition, ac impedance measurements have demonstrated increased Li diffusion in nanosized materials.[10] MnO_2 is also important in numerous catalytic processes. An example of which is its application in electrochemical ORRs, which are essential in a variety of energy storage and conversion applications including metal−air batteries and fuel cells.[4,11] This technology is the basis of the Li−O_2 battery system, which is an alternative to conventional Li-ion batteries and could potentially significantly increase specific energy density.[12] An overview of other catalytic applications of manganese oxides is available elsewhere.[13] Nanostructured β-MnO_2 also shows potential as a supercapacitor electrode material.[14,15] Upon nanostructuring of the material, a significant increase in the capacitance (285 F g^{-1})[14,15] is observed when compared to the bulk material. It has been proposed that the cause of this dramatic increase in capacitance is a result of the greater surface area exposure as a result of the nanostructuring.[13]

Despite the clear importance of nanostructuring of this material, the understanding of how it drastically improves many of its electrochemical properties is still lacking. It is only recently that the interfaces of this material have been analyzed in any great detail. So far, the primary focus has been on surfaces.[13,16−21] Tompsett et al.[13,16] used density functional theory (DFT) with the generalized gradient approximation (GGA) and Hubbard U corrections to consider the importance of surface to bulk Li-ion migration as well as the structure of numerous β-MnO_2 surfaces and the effect oxygen vacancy formation has on the catalytic properties of these surfaces. They found that the formation energies of oxygen vacancies and Mn reduction were low compared to the bulk and other rutile structures which suggests high electrochemical performance of β-MnO_2 surfaces. Mellan et al.[17] used the same computational approach for calculating lithium and oxygen adsorption at the (110) surface of β-MnO_2. Studies by Oxford and Chaka[18,19] use

Received: October 22, 2014
Accepted: January 6, 2015
Published: January 6, 2015

DOI: 10.1021/am507273c
ACS Appl. Mater. Interfaces 2015, 7, 1726−1734

the GGA without U corrections to study heavily oxidized and reduced low index surfaces as well as the effects of surface hydration. The catalytic activity of β-MnO_2 surfaces for application in ORRs has also been assessed using DFT simulations.[4,20]

In a previous study,[21] we used interatomic potential methods to investigate the lowest energy structures for a number of β-MnO_2 grain boundaries (GBs) and then proceeded to calculate the energies of Mn^{4+} reduction and oxygen vacancy formation. Both reduction and oxygen formation energies were shown to be favored in and around the GB core suggesting a potentially higher catalytic activity at the GBs. The Σ 5(210)/[001] GB was also shown to be the most stable out of those tested. It is not yet known what the concentration of GBs is in these nanostructured β-MnO_2 samples. While GBs will play a more significant role in determining the properties of bulk samples, the GB concentration in the more electrochemically active nanostructured samples will be significantly reduced. However, GBs adjacent to the highly active surfaces in these samples are likely to be important in influencing the electrochemical properties. Given the importance of electronic structure, oxygen vacancy formation and reduction in the electrochemical applications that have been described, it is important that a study with the focus on GBs is completed to complement previous surface and bulk studies.

In this study, we use GGA+U calculations to analyze the atomic and electronic structure of the β-MnO_2 Σ 5(210)/[001] GB. We then assess the effect of cation reduction and oxygen vacancy formation on these structures and the potential catalytic activity of the GB. We begin by describing our computational approach and justifications for using such methods. This is followed by details of the GB local structure and stability as well as a discussion of its electronic structure. Finally, we consider oxygen vacancy formation at the GB and determine the consequences for electrochemical performance from the defect energetics, electronic structures and charge analysis.

2. METHODOLOGY

When low symmetry structures with complex electronic and magnetic properties are considered, the accuracy of DFT calculations is often essential. However, because of their computational expense, it is sometimes necessary to begin by using a more computationally efficient technique. Building upon our previous work,[21] we use interatomic potentials to find the lowest energy GB structures. These selected structures can then be simulated using DFT to better describe their complex properties. For the interatomic potentials calculations, the interionic interactions are simulated using the Born model for ionic solids. In this model ions are treated as charged spheres where the short-range forces are accounted for by the interatomic potentials and the long-range ionic interactions are treated using Coulombic terms. The methods discussed in this section are well established, and comprehensive reviews are available elsewhere.[22] We use the proven potential model of Maphanga et al.[23,24] This model has been successfully used for a number of studies of β-MnO_2[9,25] and has recently been used to find the lowest energy surface structures of the material,[13] which were then used as starting points for ab initio calculations, as done for this work also. The model reproduces the lattice parameters of the bulk β-MnO_2 structure to within 2% of experiment. All interatomic potential calculations in this work were completed using the General Utility Lattice Program (GULP).[26]

The lowest energy Σ 5(210)/[001] GB structure was tested using DFT+U calculations with the GGA[27] and projector augmented-wave (PAW)[28] methods. All ab initio calculations were completed using the VASP[29] code. We use a cutoff energy of 500 eV for all calculations. A k-point grid of 2 × 2 × 3 was used for the GB supercell calculations. The value of the U parameter used for our calculations was chosen on the basis of previous work on β-MnO_2 surfaces.[13,16] The values were determined using Wien2k[30,31] and have been shown to accurately describe Li intercalation, band gaps and magnetic interactions.[13] However, it is only when the U parameter is applied in the fully localized limit that such descriptions are achieved. Further details on the impact of the values and nature of the U parameter on this material are available in a previous publication.[32] The fully localized limit is used in this work and we employ values of $U - J$ = 5.1 eV, for the spherical part of the interaction, and J = 1.0 eV. A collinear antiferromagnetic ordering is used in all our calculations. This ordering is the lowest energy magnetic configuration[32,33] for the rutile cell, but is not the lowest for this oxide as there is a noncollinear screw-type magnetic structure below 92 K.[34] The calculated total energies are unlikely to be affected by this difference because of the weak coupling indicated by the low transition temperature to paramagnetism.[17] The crystal and magnetic structures used in this work are illustrated for the bulk and GB structures in Figure 1. The lattice parameters calculated using GGA+U (a = 4.439 Å, c = 2.932 Å) are within 2% of the experimental values (a = 4.398 Å, c = 2.873 Å).[35]

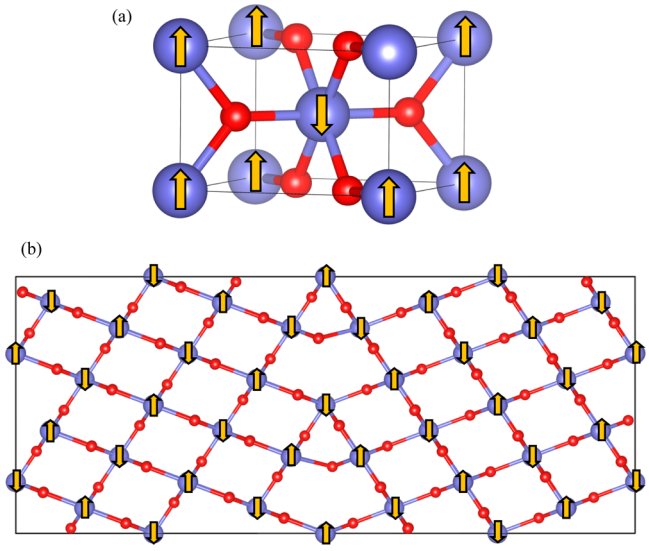

Figure 1. Unoptimized crystal structures of (a) bulk β-MnO_2 and (b) the β-MnO_2 Σ 5(210)/[001] GB. The arrows represent spin polarization indicating the magnetic arrangement used in the calculations. Red spheres represent oxygen ions and blue spheres represent manganese ions.

The Σ 5(210)/[001] GB was chosen for this work, as it is commonly observed in rutile structures and has been featured in numerous studies of TiO_2 GBs.[36−38] It has also recently been shown to be significantly more stable than various other GBs in β-MnO_2.[21] The starting GB configuration is formed using coincident site lattice (CSL) theory. A common problem with simulating GBs is that there are often ions with the same charge in close proximity at the boundary which leads to increased Coulombic repulsion and unstable GBs. We address this issue by the common approach of exploring the γ-surface of the GBs. Using rigid body translations, one grain can be displaced with respect to the other in various three-dimensional translation states. This method is crucial in finding the global minimum and works by calculating the GB energy at each translation. The GB energy is calculated by

$$\sigma_{GB} = \frac{E_{GB} - E_{bulk}}{2A} \quad (1)$$

where E_{GB} and E_{bulk} are the energies of the GB and the bulk supercell respectively, and A is the area of the interface. The area of the interface is doubled to account for the presence of the two equivalent GBs in

DOI: 10.1021/am507273c
ACS Appl. Mater. Interfaces 2015, 7, 1726−1734

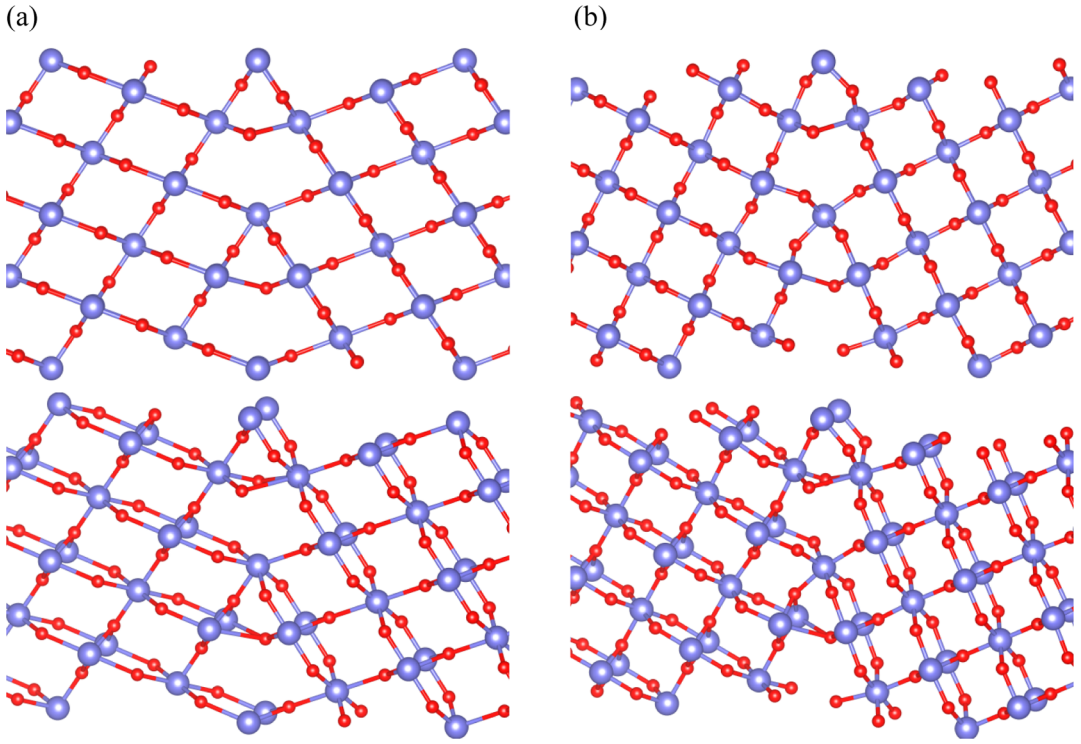

Figure 2. Crystal structures of (a) the unoptimized, starting β-MnO_2 Σ 5(210)/[001] GB configuration and (b) the optimized, lowest energy final β-MnO_2 Σ 5(210)/[001] GB configuration.

the supercell. The energy was calculated as a function of translation states with increments of about 0.01 nm. This approach has been used for simulations of GBs in many different materials.[39−42] The GB supercell has dimensions of a = 5.82 Å, b = 13.96 Å and c = 33.76 Å with a total of 288 ions.

Vacancy formation energies in this work are calculated from the following reduction reaction:

$$O_O^x + 2Mn_{Mn}^x \rightarrow V_O^{\bullet\bullet} + 2Mn_{Mn}' + \frac{1}{2}O_{2(g)} \quad (2)$$

In all our calculations, we assume a reduction cluster where the two reduced Mn ions neighbor the oxygen vacancy. A similar approach was taken in our previous work.[21] To calculate the defect formation energy of an oxygen vacancy, the energy of a reference isolated spin triplet oxygen molecule must also be calculated. This is achieved by simulating the oxygen molecule in a large cubic cell using the same calculation conditions used for the GB calculations. We obtain an energy of −9.09 eV for the oxygen molecule. It must be noted that DFT calculations are often affected by the well-known inability to correctly describe the O_2 binding energy leading to significant overstabilization of the O_2 molecule. To estimate this error we follow the procedure of Tompsett et al.[13] whereby Mn reduction and oxygen vacancy formation are both considered in the following reaction:

$$MnO_2 \rightarrow \frac{1}{2}Mn_2O_3 + \frac{1}{4}O_{2(g)} \quad (3)$$

By combining the reaction enthalpy calculated using the GGA+U with the experimental enthalpy (40 kJ mol^{-1}),[43] we obtain a correction value of 1.08 eV. This value is applied to all the oxygen vacancy formation energies reported in this work.

3. RESULTS AND DISCUSSION

3.1. Stability and Structure of the Stoichiometric Σ 5(210)/[001] GB. It is well-known that the electronic properties of semiconductor materials are largely influenced by GBs and the high concentration of defects that exist at these interfaces. However, before discussing the electronic and defective structures, it is essential that we assess the stability of our stoichiometric GB model and analyze its local structure. As discussed previously, we could find very little experimental analysis of the local structure of β-MnO_2 GBs, so comparisons in this section are made to previous computational works and rutile TiO_2.

Crystal structures of the GB before and after optimization and translations are given in Figure 2. Our GGA+U calculated interfacial energy for the Σ 5(210)/[001] GB is 0.36 J m^{-2}. This value is considerably lower than the value obtained for the same GB using interatomic potentials (1.53 J m^{-2}). Although the energy difference between these two methods is large, it is not uncommon for DFT calculations to predict significantly more stable GBs compared to lattice statics for some materials.[42] Testing also confirmed a similar energy difference between the lattice statics and DFT values for the Σ 5(310)/[001] MnO_2 GB. This strongly suggests that DFT is better at producing more stable GB structures for this material compared to classical methods. The Σ 5(210)/[001] MnO_2 GB is far more stable than its equivalent structure in rutile TiO_2 when calculated using both ab initio and interatomic potential methods.[36−38] DFT calculations by Körner and Elsässer[36] give a Σ 5(210)/[001] GB energy of 1.92 J m^{-2}. Dawson et al.[37] also used DFT to calculate an energy of 1.72 J/m^{-2} for the Σ 5(210)/[001] GB. This value is marginally higher than the value of 1.70 J m^{-2} calculated using interatomic potential methods.[39] There are numerous reasons as to why such a difference in GB energies is observed. These include insufficient cell sizes used in the previous calculations and the fact that two different rutile structured materials will not have the exact same GB energies. It is also possible that rigid body translations were not considered in some of the previous works.

Comparison of Figure 2a,b shows that the translations applied to this GB to achieve the lowest energy structure are

DOI: 10.1021/am507273c
ACS Appl. Mater. Interfaces 2015, 7, 1726−1734

subtle. This to be expected given that the Mn−O interatomic distances at the GB of the initial structure are similar to that of the bulk (1.88 and 1.90 Å), and it also explains why this boundary is low in energy. This is not true for other β-MnO_2 GBs, where octahedral distortion and undercoordination are common and the energy is therefore considerably higher.[21] The Mn−O bond distances for ions closest to the GB core are illustrated in Figure 3. Although there is some distortion of the

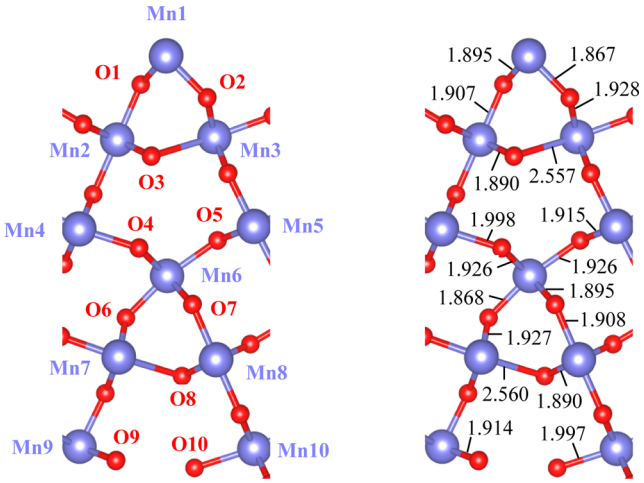

Figure 3. Illustration of the optimized Mn−O bond distances (Å) for ions closest to the Σ 5(210)/[001] GB core.

octahedra at the GB, most coordination of the ions is preserved. However, two of the oxygen ions are overcoordinated, as is the Mn3 ion. The O3 and O8 ions have increased 4-fold coordination, and the Mn3 ion has 7-fold coordination. This results in long Mn3−O3 and Mn7−O8 bonds, which measure 2.557 and 2.560 Å, respectively. It has been previously been reported that undercoordinated oxygen ions at the surface are likely to be adsorption sites for hydrogen when the material is used as a supercapacitor electrode,[13] so indeed the opposite is likely true for overcoordinated oxygen ions. The majority of bonds have been lengthened or shortened compared to the equilibrium bulk values, but only by a small margin. Our structure is in good agreement with previous works[39,40] in that it shows no significant rigid-body contraction or expansion.

3.2. Electronic Structure of the Stoichiometric Σ 5(210)/[001] GB. Figure 4 shows the calculated total density of states (TDOS) for the β-MnO_2 perfect crystal and the Σ 5(210)/[001] GB. Local partial DOS (PDOS) for Mn3 and Mn7 ions and O3 and O8 ions at the GB core are also displayed. For all these plots, the zero is aligned with uppermost occupied state at the top of the valence band. The formal oxidation state of Mn is β-MnO_2 is 4+. Octahedral field splitting means the energies of the 3d orbitals of the Mn^{4+} ions are divided into t_{2g} and e_g symmetry states with an electronic configuration of t_{2g}^3 e_g^0. The t_{2g} majority states are occupied, while the e_g majority states are empty.

Although the general shape of the TDOS for the bulk crystal and the GB are similar, there are important differences. β-MnO_2 is a semiconducting material with a small bandgap[44] that has not yet been experimentally determined. Our calculated value of 0.7 eV is in qualitative agreement with this and is also in good agreement with previous GGA+U calculations (0.8 eV).[32] The importance of using Hubbard U corrections with full anisotropy for analyzing the electronic properties of this

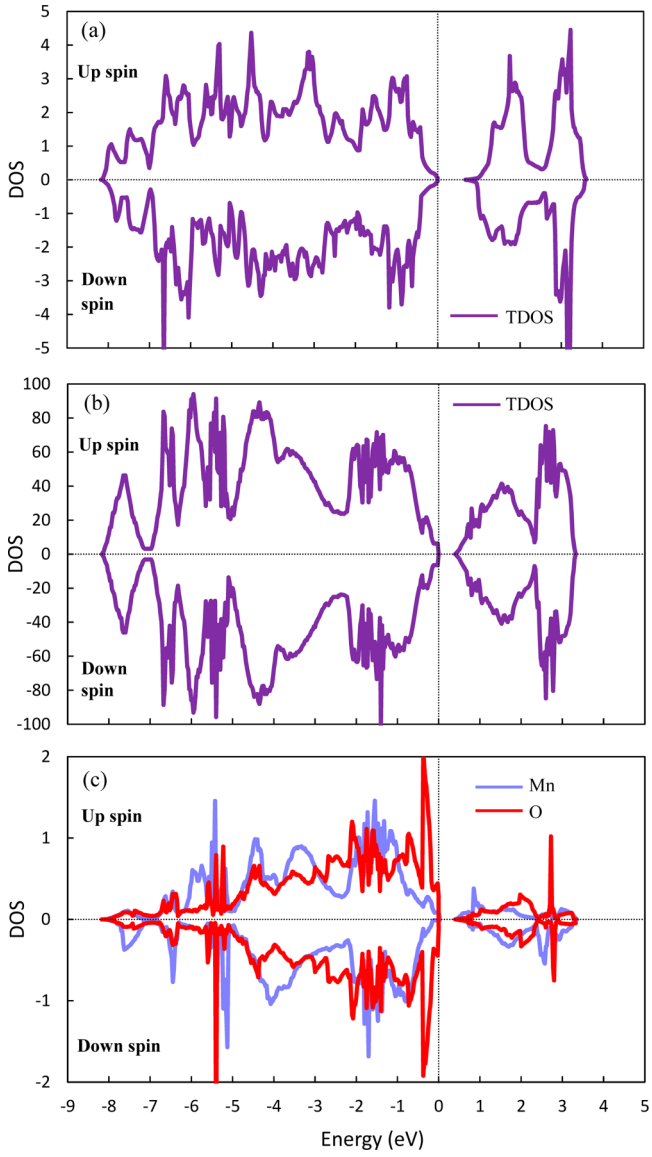

Figure 4. Total DOS for the (a) β-MnO_2 perfect crystal, (b) β-MnO_2 Σ 5(210)/[001] GB and (c) combined local PDOS for the Mn3, Mn7, O3 and O8 ions (as labeled in Figure 3) at the Σ 5(210)/[001] GB core.

material has recently been assessed.[32] The results show that the use of the "effective" U correction cannot reproduce the bandgap and yields a metallic DOS. Figure 4(b) shows that the GB structure produces extra electronic states in the bandgap which results in the bandgap being reduced to 0.4 eV. Reduced bandgaps have also been observed for β-MnO_2 surfaces.[45] In addition, these surfaces were found to be metallic.

To find the origin of these additional states we carried out local PDOS analysis on ions near the GB, with particular focus on the overcoordinated ions. Overcoordination of two oxygen ions at the GB core produces a sharp 2p state near the valence band maximum, clearly shown by Figure 4c. This overcoordination influences the electronic nature of the bonded Mn ions and causes the formation of extra gap states near the bottom of the conduction band. In addition to overcoordination, other common features in GBs like bond bending, stretching and shortening can also have a dramatic effect on the electronic structure. However, distinguishing the

DOI: 10.1021/am507273c
ACS Appl. Mater. Interfaces 2015, 7, 1726−1734

individual contribution of each of these factors is difficult. Similar results have recently been observed for a $LiCoO_2$ twin boundary[46] where the different bonding natures of oxygen ions at the boundary cause the formation of additional states in the bandgap near both the valence band maximum and conduction band minimum. It was also suggested that such results indicate localized states at the interface plane which could provide local electron conduction at the GB core. Bader charge analysis shows a charge transfer from the O3 ion to the Mn3 ion and from the O8 ion to the Mn7 ion. The bulk oxygen Bader charge is 7.12 electrons (PAW_GGA pseudopotential has 6 electrons) which is reduced to 7.03 for both O3 and O8. For bulk Mn, the Bader charge is 4.76 electrons (PAW_GGA pseudopotential has 7 electrons), which increases to 4.94 for both Mn3 and Mn7. This suggests an increase in covalent character or weak metal−metal interactions. Similar interactions have previously been shown to influence bulk magnetic properties.[32]

3.3. Oxygen Vacancy Formation and Catalytic Activity at the Σ 5(210)/[001] GB. The formation of oxygen vacancies and the reduction of Mn^{4+} to Mn^{3+} are essential for the catalytic applications of MnO_2. Many previous wroks have examined the importance of these defects for catalyzed reactions like ORRs[4,47−49] and the enhancement they can have on catalytic performance.[4,13] To date the most comprehsive study of oxygen vacancy formation at the interfaces of β-MnO_2 is the work of Tompsett et al.[13] where DFT+U was used to calculate formation energies for a number of β-MnO_2 surfaces. Oxygen vacancy energies for each surface simulated were lower than the respective value obtained for the bulk material. Furthermore, the calculated values were lower than those for rutile TiO_2 surfaces. It is suggested that such favorable oxygen vacancy defects may play a signifcant role in the favorable catalytic performance of β-MnO_2. While other studies have considered oxygen vacancies with high oxygen vacancy concentrations,[18,19] it is thought that it is dilute, low concentration, oxygen vacancies that are most important for catalytic properties. In this work, we carry out the first ab initio study of oxygen vacancies in a β-MnO_2 GB. We compare our results to DFT calculations for the bulk and surface structures as well as interatomic potential calculations for several GB structures.

The oxygen vacancy defect formation energies for the Σ 5(210)/[001] GB using eq 2 are given in Table 1. The formation energy calculated for the bulk material is 2.75 eV, this value is larger than all those calculated for the potential vacancy sites in the GB. This suggests that GBs are likely to be far more catalytically active than the bulk. Given the differences between the methodologies used, comparison previous lattice statics calculations is purely qualitative, however the previous also show facile oxygen vacancy formation for a series of β-MnO_2 GBs including Σ 5(210)/[001].[21] The results are also similar to those of Tompsett et al.[13] where oxygen vacancy formation is favored at β-MnO_2 surfaces. It is noteworthy that for the O2 and O6 sites, the oxygen vacancy formation energies are lower than any calculated for the surface structures. The difference in formation energy between these two sites and our calculated bulk value is also significantly larger than any energy difference between the surface and bulk oxygen sites calculated by Tompsett et al. It is currently unclear how the contribution of the GBs to the catalytic properties compares to that of the surfaces, especially for nanostructured samples. This topic will be discussed in a subsequent publication.

Table 1. Oxygen Vacancy Formation Energies Based on eq 2 for the β-MnO_2 Σ 5(210)/[001] GB[a]

oxygen site	ΔE_F (eV)
O1	2.23
O2	0.71
O3	1.89
O4	2.47
O5	2.45
O6	0.70
O7	2.33
O8	1.88
O9	2.43
O10	2.44
bulk	2.75

[a]Oxygen ions are labelled according to Figure 3.

The majority of the calculated oxygen formation energies are similar (2.23−2.47 eV). The exceptions are the O2, O3, O6 and O8 sites, which are now discussed in more detail. The O3 and O8 ions are overcoordinated and bonded to four Mn ions; this results in each ion having two standard length Mn−O bonds and two weaker, longer Mn−O bonds with more covalent character. These weaker bonds and the distortion to the lattice caused by the overcoordination results in the lower oxygen vacancy formation energies of 1.88−1.89 eV. The O2 and O6 ions have the lowest vacancy formation energies calculated. Although all ions at the GB experience some local distortion, the distortion is much greater around these two ions. Figure 5a shows the local structure of the standard tricoordinated oxygen ion in bulk β-MnO_2. Figure 5b,c shows the local structure of the tricoordinated O2 and O6 ions, respectively. In the bulk structure, a perfect 360° trigonal planar is observed, whereas for the O2 and O6 ions in the GB structure, this geometry is significantly distorted, resulting in a reduction of the total coordination angle of ∼16°. In addition, bulk oxygen coordination consists of one longer Mn−O bond (1.90 Å) and two shorter Mn−O bonds (1.88 Å). This is reversed for the O2 and O6 ions, where instead only one shorter, stronger bond is formed along with two longer, weaker bonds. It is this distortion that results in the low vacancy formation energies calculated for these two oxygen ions.

3.4. Electronic Structure of the Oxygen Deficient Σ 5(210)/[001] GB. Analysis of the oxygen deficient GB electronic structure reveals that the change in the nature of the bandgap is very much dependent upon the oxygen ion removed. Although the removal of most oxygen ions results in additional spin-polarized gap states (thus reducing the bandgap even further), the removal of the O4 ion actually causes a small increase in the bandgap of the GB DOS. The TDOS for the O4 and O6 vacant structures are displayed in Figure 6. These two vacancies have been chosen for further discussion as they exhibit different results with regard to the bandgap and also have the highest and lowest vacancy formation energies, respectively. The removal of O4 produces a bandgap of 0.45 eV, 0.05 eV larger than the stoichiometric GB, whereas the removal of O6 has no effect on the bandgap size. Other vacancies cause reductions in the bandgap of between 0.05 and 0.2 eV. Another interesting feature of these TDOS is the half-metallic behavior. This is clear from the fact that in the bandgap, the spin-up states are insulating, while the spin-down states are conducting. Similar electronic behavior is also observed for the other oxygen vacancies. Metallic behavior has also been calculated for the oxygen-deficient β-MnO_2 (311)

DOI: 10.1021/am507273c
ACS Appl. Mater. Interfaces 2015, 7, 1726−1734

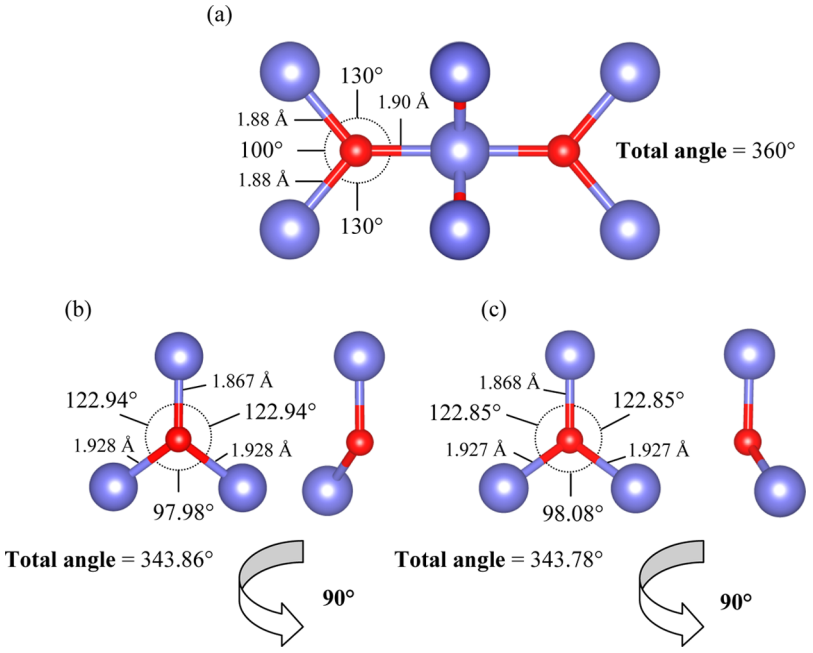

Figure 5. Illustrations of the local structure of (a) an oxygen ion in bulk β-MnO_2, (b) the O2 ion in the β-MnO_2 Σ 5(210)/[001] GB and (c) the O6 ion in the β-MnO_2 Σ 5(210)/[001] GB.

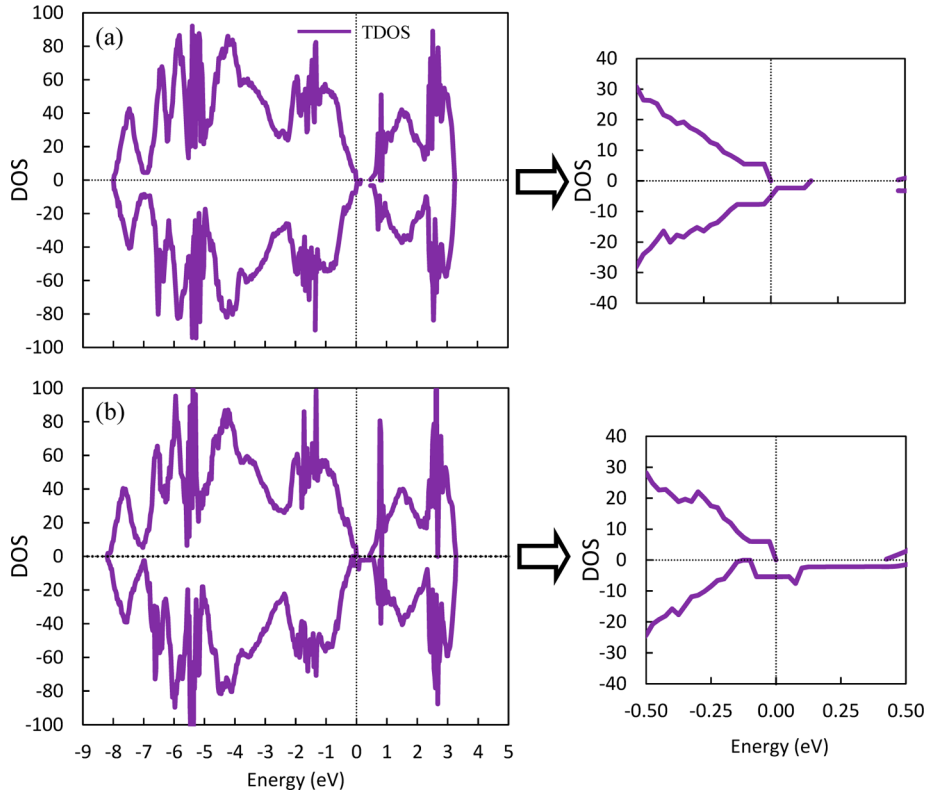

Figure 6. TDOS for the β-MnO_2 Σ 5(210)/[001] GB with (a) an O4 vacancy and (b) an O6 vacancy. Plots showing the bandgap in more detail are provided on the right.

surface by Tompsett et al.[13] and for a variety of stoichiometric β-MnO_2 surfaces.[45] It has also been reported in experimental studies of bulk[44] and nanocrystalline[50] samples with oxygen vacancies. Given that the bandgap of this material is small, one could expect that the formation of metallic states is low in energy.

In addition to β-MnO_2, half-metallicity has previously been observed in the surfaces of a number of metal oxides.[51] Recently, it has also been confirmed in the surfaces[52] and GBs[53] of Li_2O_2. The half-metallic behavior in these materials results from the loss of coordination and charge depletion of oxygen ions at oxygen-rich surfaces, resulting in the formation of 2p holes in the valence band. Given that this behavior is usually

DOI: 10.1021/am507273c
ACS Appl. Mater. Interfaces 2015, 7, 1726−1734

present in oxygen-rich/terminated surfaces, cation vacancies are also found to induce metallicity.[51] However, as it is oxygen vacancies in this work causing the metallic behavior, it is unlikely that such a mechanism is true, as the charge resulting from the oxygen vacancy should become localized on the Mn ions, causing them to be reduced. It is interesting that even Li-rich polar surfaces have been shown to exhibit nonmagnetic metallic behavior also.[52] Half-metallicity is common in many other stoichiometric and oxygen deficient metal oxide systems containing *d* electrons.[54−57] As with the overcoordinated oxygen ions in the stoichiometric GB, such behavior may result in enhanced conductivity localized at the GBs. Furthermore, it is important that this behavior is observed not only for the oxygen ions with the most distorted local chemical environment (e.g., O6), but also ions with high vacancy formation energy and almost bulk-like local structures (e.g., O4). To further investigate this phenomenon, we analyze the charge density isosurfaces of the oxygen deficient GBs and carry out Bader charge analysis.

Isosurfaces of the charge density difference for the O4 and O6 deficient GB structures are given in Figure 7. These were computed from the density of the vacancy defect system plus the spherically symmetrized density of an isolated gaseous triplet oxygen atom placed at the vacancy position, minus the density of the defect-free system. In bulk β-MnO_2, the excess charge density is localized on the two nearest Mn ions to the oxygen vacancy. This is in full agreement with eq 2 with two Mn ions becoming reduced to achieve charge compensation. Similar results are reported for DFT calculations of the β-MnO_2 (110), (001) and (211) surfaces.[13] The charge density isosurfaces for the oxygen deficient GB structures exhibit very different behavior to the bulk. The charge is delocalized over many Mn and O ions as the GB and becomes metallic upon vacancy formation. Similar behavior was also observed for the β-MnO_2 (311) surface.[13] This charge is primarily confined to the GB region meaning that these interfaces could potentially assist the supply of electrons during catalytic reactions. Bader charge analysis also shows that the charge is spread over a number of Mn and oxygen sites at the GB. However, despite the charge delocalization, the closest Mn ions to the vacancy sites still possess the largest distribution of charge resulting from the vacancy formation with values of ∼5 electrons (compared to 4.76 electrons in the bulk). There is no significant charge depletion of oxygen vacancies close to the vacancy site as has been recently calculated for Li_2O_2 surfaces[52] and GBs.[53] Any minor charge depletion of oxygen ions remains reasonably consistent over the majority of oxygen ions at the GB.

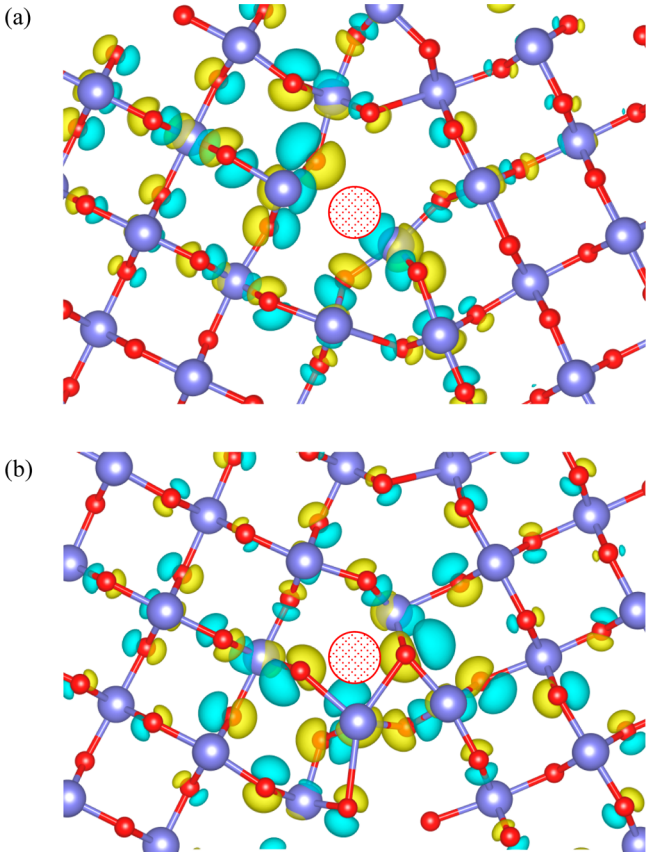

Figure 7. Charge density difference isosurfaces for the β-MnO_2 Σ 5(210)/[001] GB with (a) an O4 vacancy and (b) an O6 vacancy. The yellow regions represent charge accumulation and the blue areas represent charge depletion. The large red circle indicates the position of the oxygen vacancy.

4. CONCLUSIONS

GGA+U calculations have been employed to study the structural and electronic properties of the β-MnO_2 Σ 5(210)/[001] GB. We consider both the stoichiometric GB and the formation of oxygen vacancies. The GB structure is found to be stable with little distortion and most ion coordination preserved. Some ions are, however, found to be over-coordinated. The electronic GB structure has additional states within in the bandgap compared to the pristine structure, which results in a 0.3 eV reduction of the bandgap. These localized states are found to be caused by the overcoordinated ions at the GB and may produce electronic conduction pathways that are confined to the interface. Bader charge analysis shows that the longer bonds formed as a result of overcoordination are covalent in character. Oxygen vacancy formation energies (with the resulting reduction of Mn ions) are found to be lower for all GB oxygen sites compared to bulk β-MnO_2. Some energies are also lower than values recently calculated for β-MnO_2 surfaces. Our results suggest there is high catalytic activity at the GBs of this material. The majority of oxygen vacancies produce additional spin-polarized gap states, meaning a further reduction in the bandgap; conversely, some vacancies actual no such reduction and some marginally increase the bandgap. All oxygen vacancies produce metallic behavior at the GB, which creates potential for enhanced conductivity that is localized at the GBs.

AUTHOR INFORMATION

Corresponding Author

*J. A. Dawson. E-mail: dawson.jamesalexander.2w@kyoto-u.ac.jp. Tel.: +81-75-753-5435.

Notes

The authors declare no competing financial interest.

ACKNOWLEDGMENTS

The authors thank the Japan Society for the Promotion of Science (JSPS) for funding through Grants-in-Aid for (a) Scientific Research on Innovative Areas "Nano Informatics" (Grant No. 25106005) and for (b) JSPS fellows (Grant No. 2503370).

DOI: 10.1021/am507273c
ACS Appl. Mater. Interfaces 2015, 7, 1726−1734

REFERENCES

(1) Wang, D.; Liu, L.-M.; Zhao, S.-J.; Li, B.-H.; Liu, H.; Lang, X.-F. β-MnO_2 as a Cathode Material for Lithium Ion Batteries from First Principles Calculations. *Phys. Chem. Chem. Phys.* **2013**, *15*, 9075−9083.

(2) Armstrong, A. R.; Bruce, P. G. Synthesis of Layered $LiMnO_2$ as an Electrode for Rechargeable Lithium Batteries. *Nature* **1996**, *381*, 499−500.

(3) Armstrong, A. R.; Holzapfel, M.; Novák, P.; Johnson, C. S.; Kang, S.-H.; Thackeray, M. M.; Bruce, P. G. Demonstrating Oxygen Loss and Associated Structural Reorganization in the Lithium Battery Cathode $Li[Ni_{0.2}Li_{0.2}Mn_{0.6}]O_2$. *J. Am. Chem. Soc.* **2006**, *128*, 8694−8698.

(4) Cheng, F.; Zhang, T.; Zhang, Y.; Du, J.; Han, X.; Chen, J. Enhancing Electrocatalytic Oxygen Reduction on MnO_2 with Vacancies. *Angew. Chem., Int. Ed.* **2013**, *52*, 2474−2477.

(5) Jiao, F.; Bruce, P. G. Mesoporous Crystalline β-MnO_2—A Reversible Positive Electrode for Rechargeable Lithium Batteries. *Adv. Mater.* **2007**, *19*, 657−660.

(6) Thackeray, M. M.; Johnson, C. S.; Vaughey, J. T.; Li, N.; Hackney, S. A. Advances in Manganese-Oxide "Composite" Electrodes for Lithium-Ion Batteries. *J. Mater. Chem.* **2005**, *15*, 2257−2267.

(7) Luo, J.-Y.; Zhang, J.-J.; Xia, Y.-Y. Highly Electrochemical Reaction of Lithium in the Ordered Mesoporosus β-MnO_2. *Chem. Mater.* **2006**, *18*, 5618−5623.

(8) Cheng, F.; Zhao, J.; Song, W.; Li, C.; Ma, H.; Chen, J.; Shen, P. Facile Controlled Synthesis of MnO_2 Nanostructures of Novel Shapes and Their Application in Batteries. *Inorg. Chem.* **2006**, *45*, 2038−2044.

(9) Sayle, T. X. T.; Maphanga, R. R.; Ngoepe, P. E.; Sayle, D. C. Predicting the Electrochemical Properties of MnO_2 Nanomaterials Used in Rechargeable Li Batteries: Simulating Nanostructure at the Atomistic Level. *J. Am. Chem. Soc.* **2009**, *131*, 6161−6173.

(10) Bach, S.; Pereira-Ramos, J. P.; Willmann, P. A Kinetic Study of Electrochemical Lithium Insertion in Nanosized Rutile β-MnO_2 by Impedance Spectroscopy. *Electrochim. Acta* **2011**, *56*, 10016−10022.

(11) Kinoshita, K. *Electrochemical Oxygen Technology*; Wiley: New York, 1992.

(12) Bruce, P. G.; Freunberger, S. A.; Hardwick, L. J.; Tarascon, J.-M. Li-O_2 and Li-S Batteries with High Energy Storage. *Nat. Mater.* **2012**, *11*, 19−29.

(13) Tompsett, D. A.; Parker, S. C.; Islam, M. S. Rutile (β-)MnO_2 Surfaces and Vacancy Formation for High Electrochemical and Catalytic Performance. *J. Am. Chem. Soc.* **2014**, *136*, 1418−1426.

(14) Devaraj, S.; Munichandraiah, N. Effect of Crystallographic Structure of MnO_2 on Its Electrochemical Capacitance Properties. *J. Phys. Chem. C* **2008**, *112*, 4406−4417.

(15) Zang, J.; Li, X. *In situ* Synthesis of Ultrafine β-MnO_2/Polypyrrole Nanorod Composites for High-Performance Supercapacitors. *J. Mater. Chem.* **2011**, *21*, 10965−10969.

(16) Tompsett, D. A.; Parker, S. C.; Bruce, P. G.; Islam, M. S. Nanostructuring of β-MnO_2: The Important Role of Surface to Bulk Ion Migration. *Chem. Mater.* **2013**, *25*, 536−541.

(17) Mellan, T. A.; Maenetja, K. P.; Ngoepe, P. E.; Woodley, S. M.; Catlow, C. R. A.; Grau-Crespo, R. Lithium and Oxygen Adsorption at the β-MnO_2(110) Surface. *J. Mater. Chem. A* **2013**, *1*, 14879−14887.

(18) Oxford, G. A. E.; Chaka, A. M. First-Principles Calculations of Clean, Oxidized, and Reduced β-MnO_2 Surfaces. *J. Phys. Chem. C* **2011**, *115*, 16992−17008.

(19) Oxford, G. A. E.; Chaka, A. M. Structure and Stability of Hydrated β-MnO_2 Surfaces. *J. Phys. Chem. C* **2012**, *116*, 11589−11605.

(20) Li, L.; Wei, Z.; Chen, S.; Qi, X.; Ding, W.; Xia, M.; Li, R.; Xiong, K.; Deng, Z.; Gao, Y. A Comparative DFT Study of the Catalytic Activity of MnO_2 (2 1 1) and (2-2-1) Surfaces for an Oxygen Reduction Reaction. *Chem. Phys. Lett.* **2012**, *539*, 89−93.

(21) Dawson, J. A.; Tanaka, I. Oxygen Vacancy Formation and Reduction Properties of β-MnO_2 Grain Boundaries and the Potential for High Electrochemical Performance. *ACS Appl. Mater. Interfaces* **2014**, *6*, 17776−17784.

(22) Harding, J. H. Computer Simulation of Defects in Ionic Solids. *Rep. Prog. Phys.* **1990**, *53*, 1403.

(23) Maphanga, R. R.; Sayle, D. C.; Sayle, T. X. T.; Ngoepe, P. E. Amorphization and Recrystallization Study of Lithium Insertion into Manganese Dioxide. *Phys. Chem. Chem. Phys.* **2011**, *13*, 1307−1313.

(24) Maphanga, R. R.; Parker, S. C.; Ngoepe, P. E. Atomistic Simulation of the Surface Structure of Electrolytic Manganese Dioxide. *Surf. Sci.* **2009**, *603*, 3184.

(25) Sayle, T. X. T.; Catlow, C. R. A.; Maphanga, R. R.; Ngoepe, P. E.; Sayle, D. C. Generating MnO_2 Nanoparticles Using Simulated Amorphization and Recrystallization. *J. Am. Chem. Soc.* **2005**, *127*, 12828−12837.

(26) Gale, J. D.; Rohl, A. L. The General Utility Lattice Program (GULP). *Mol. Simul.* **2003**, *29*, 291−341.

(27) Perdew, J. P.; Burke, K.; Ernzerhof, M. Generalized Gradient Approximation Made Simple. *Phys. Rev. Lett.* **1996**, *77*, 3865.

(28) Blöchl, P. E. Projector Augmented-Wave Method. *Phys. Rev. B* **1994**, *50*, 17953.

(29) Kresse, G.; Furthmüller, J. Efficiency of Ab-initio Total Energy Calculations for Metals and Semiconductors Using a Plane-Wave Basis Set. *Comput. Mater. Sci.* **1996**, *6*, 15−50.

(30) Schwarz, K.; Blaha, P. Solid State Calculations using WIEN2k. *Comput. Mater. Sci.* **2003**, *28*, 259−273.

(31) Madsen, G. K. H.; Novak, P. Charge Order in Magnetite. An LDA+U Study. *Europhys. Lett.* **2005**, *69*, 777−783.

(32) Tompsett, D. A.; Middlemiss, D. S.; Islam, M. S. Importance of Anisotropic Coulomb Interactions and Exchange to the Band Gap and Antiferromagnetism of β-MnO_2 from DFT+U. *Phys. Rev. B* **2012**, *86*, 205126.

(33) Franchini, C.; Podloucky, R.; Paier, J.; Marsman, M.; Kresse, G. Ground-State Properties of Multivalent Manganese Oxides: Density Functional and Hybrid Density Functional Calculations. *Phys. Rev. B* **2007**, *75*, 195128.

(34) Yoshimori, A. A New Type of Antiferromagnetic Structure in the Rutile Type Crystal. *J. Phys. Soc. Jpn.* **1959**, *14*, 807−821.

(35) Baur, W. Rutile-Type Compounds. V. Refinement of MnO_2 and MgF_2. *Acta Crystallagr. B* **1976**, *32*, 2200−2204.

(36) Körner, W.; Elsässer, C. Density Functional Theory Study of Dopants in Polycrystalline TiO_2. *Phys. Rev. B* **2011**, *83*, 205315.

(37) Dawson, I.; Bristowe, P. D.; Lee, M. H.; Payne, M. C.; Segall, M. D.; White, J. A. First-Principles Study of a Tilt Grain Boundary in Rutile. *Phys. Rev. B* **1996**, *54*, 13727−13733.

(38) Sinnott, S. B.; Wood, R. F.; Pennycook, S. J. Ab Initio Calculations of Rigid-Body Displacements at the Σ5 (210) Tilt Grain Boundary in TiO_2. *Phys. Rev. B* **2000**, *61*, 15645−15648.

(39) Dawson, J. A.; Tanaka, I. Proton Incorporation and Trapping in ZrO_2 Grain Boundaries. *J. Mater. Chem. A* **2014**, *2*, 1400−1408.

(40) Dawson, J. A.; Tanaka, I. Local Structure and Energetics of Pr- and La-Doped $SrTiO_3$ Grain Boundaries and the Influence on Core-Shell Structure Formation. *J. Phys. Chem. C* **2014**, *118*, 25765−25778.

(41) Oba, F.; Ohta, H.; Sato, Y.; Hosono, H.; Yamamoto, T.; Ikuhara, Y. Atomic Structure of [0001]-Tilt Grain Boundaries in ZnO: A High-Resolution TEM Study of Fiber-Textured Thin Films. *Phys. Rev. B* **2004**, *70*, 125415.

(42) Benedek, N. A.; Chua, A. L. S.; Elsässer, C.; Sutton, A. P.; Finnis, M. W. Interatomic Potentials for Strontium Titanate: An Assessment of Their Transferability and Comparison with Density Functional Theory. *Phys. Rev. B* **2008**, *78*, 064110.

(43) Frtisch, S.; Navrotsky, A. Thermodynamic Properties of Manganese Oxides. *J. Am. Chem. Soc.* **1996**, *79*, 1761−1768.

(44) Sato, H.; Enoki, T.; Isobe, M.; Ueda, Y. Transport Properties and Magnetism of a Helically Hund-Coupled Conductor: β−MnO_2. *Phys. Rev. B* **2000**, *61*, 3563.

(45) Tompsett, D. A.; Islam, M. S. Surfaces of Rutile MnO2 Are Electronically Conducting, Whereas the Bulk Material Is Insulating. *J. Phys. Chem. C* **2014**, *118*, 25009−25015.

(46) Moriwake, H.; Kuwabara, A.; Fisher, C. A. J.; Huang, R.; Hitosugi, T.; Ikuhara, Y. H.; Oki, H.; Ikuhara, Y. First-Principles

DOI: 10.1021/am507273c
ACS Appl. Mater. Interfaces 2015, 7, 1726−1734

Calculations of Lithium-Ion Migration at a Coherent Grain Boundary in a Cathode Material, $LiCoO_2$. *Adv. Mater.* **2013**, *25*, 618−622.
(47) Stampfl, C.; Ganduglia-Pirovano, M. V.; Reuter, K.; Scheffler, M. Catalysis and Corrosion: The Theoretical Surface-Science Context. *Surf. Sci.* **2002**, *500*, 368−394.
(48) Wei, C.; Yu, L.; Cui, C.; Lin, J.; Wei, C.; Mathews, N.; Huo, F.; Sritharan, T.; Xu, Z. Ultrathin MnO_2 Nanoflakes as Efficient Catalysts for Oxygen Reduction Reaction. *Chem. Commun.* **2014**, *50*, 7885−7888.
(49) Cao, Y. L.; Yang, H. X.; Ai, X. P.; Xiao, L. F. The Mechanism of Oxygen Reduction on MnO_2-Catalyzed Air Cathode in Alkaline Solution. *J. Electroanal. Chem.* **2003**, *557*, 127−134.
(50) Luo, F.; Song, W.; Yan, C.-H. Enhanced Room Temperature Magnetoresistance Effect in Oxygen Defective β-MnO_2 Microcrystal. *Chem. Phys. Lett.* **2006**, *431*, 337−340.
(51) Gallego, S.; Beltran, J. I.; Cerda, J.; Munoz, M. C. Magnetism and Half-Metallicity at the O Surfaces of Ceramic Oxides. *J. Phys.: Condens. Matter* **2005**, *17*, L451.
(52) Radin, M. D.; Rodriquez, J. F.; Tian, F.; Siegel, D. J. Lithium Peroxide Surfaces Are Metallic, While Lithium Oxide Surfaces Are Not. *J. Am. Chem. Soc.* **2012**, *134*, 1093−1103.
(53) Geng, W. T.; He, B. L.; Ohno, T. Grain Boundary Induced Conductivity in Li_2O_2. *J. Phys. Chem. C* **2013**, *117*, 25222−25228.
(54) Coey, J. M. D.; Venkatesan, M. Half-Metallic Ferromagnetism: Example of CrO_2. *J. Appl. Phys.* **2002**, *91*, 8345.
(55) Szotek, Z.; Temmerman, W. M.; Kodderitzsch, D.; Hergert, W.; Svane, A.; Petit, L.; Stocks, G. M.; Winter, H. SIC-LSD Description of Half-Metallic Transition Metal Oxides. *Mol. Phys. Rep.* **2003**, *38*, 11−19.
(56) Saini, H. S.; Singh, M.; Reshak, A. H.; Kashyap, M. K. Accounting Oxygen Vacancy for Half-Metallicity and Magnetism in Fe-Doped CeO_2 Dilute Magnetic Oxide. *Comput. Mater. Sci.* **2013**, *74*, 114−118.
(57) Wu, H.; Ma, Y.; Qian, Y.; Kan, E.; Lu, R.; Liu, Y.; Tan, W.; Xiao, C.; Deng, K. The Effect of Oxygen Vacancy on the Half-Metallic Nature of Double Perovskite Sr_2FeMoO_6: A Theoretical Study. *Solid State Commun.* **2014**, *177*, 57−60.

DOI: 10.1021/am507273c
ACS Appl. Mater. Interfaces 2015, 7, 1726−1734